3D Real Time Orbital Tracking

Fabian Wehnekamp

03.09.2012

3D Real Time Orbital Tracking

Masterarbeit aus dem Fachgebiet

Physikalische Chemie

von

B.Sc. Fabian Wehnekamp
geboren am 24.06.1988
in Detmold

für die Masterprüfung in Chemie an der
Ludwig-Maximilians-Universität München

Datum der mündlichen Prüfung: 01.02.2012
Beginn der Masterarbeit: 01.03.2012
Masterarbeit beim Prüfungsausschuss eingereicht: 03.09.12

Erklärung

Ich versichere, dass ich die vorgelegte Masterarbeit am Department Chemie unter der Anregung und Anleitung von Prof. Don C. Lamb, PhD selbständig durchgeführt habe und keine anderen als die angegebenen Hilfsmittel und Quellen benutzt habe.

München, den 03.09.2012

Erstgutachter: Prof. Don C. Lamb, PhD

Zweitgutachter: Prof. Christoph Bräuchle

Acknowledgements

First of all I would like to thank Prof. Don C. Lamb for the chance to write my thesis in his work group. His constant encouragement and support through the whole thesis was a pleasure.

I would like to thank Aurélie for her advice, the answers to all of my question and the correction of my thesis. Vive la France!

I would also like to thank FAB Lab, the Michaelis and Bräuchle groups for all the help during the thesis, for great official or non official lab outings, for barbecues and the awesome atmosphere in the group. Special thanks to the boulder team: Ellen, Lena, Sushi, Waldi and Jelle for the trip to belgium and the weekly workout!

Thanks to ISS for the most outstanding answer to a support request: "Once you now how to do it, it is pretty straightforward!"

Finally I would like to thank my friends and my family: Andrea, Burckhard, Dierk, Miriam, Fiona, Jonas, Tobias, Hildegard and Helmut for their constant support, happy moments and especially my mother Andrea who told me to apply for the LMU...

Contents

List of Figures

List of Tables

Introduction

In 1665 Robert Hooke introduced the term "cell" to the scientific community by looking at cork with a conventional light microscope [1]. During the last centuries, scientists developed and used more advanced methods to resolve structures in the microscopic world with higher spatial resolution. This technical improvement was the base for more breathtaking discoveries, for example the structure of DNA by Watson, Crick, Wilkins and Franklin by x-ray crystallography [2].

To understand biochemical processes in cells it is necessary to resolve individual structures, which are significantly smaller than a single cell. The resolution of conventional microscopes is limited by the diffraction limit which was first described by Ernst Abbe in 1873 [3]:

$$\Delta x = \frac{\lambda}{2NA} \tag{1}$$

The resolution Δx is given by the ratio between the wavelength λ of the used light over the numerical aperture (NA), the ability of the objective to collect photons. Even with modern objectives (NA $\geq$1.4) the resolution limit for visible light is between 200 to 350 nm. This means that normal microscopy is not sufficient to resolve structures in the nm range or single proteins.
The diffraction limit can be overcome by the so-called super resolution techniques. With post-processing of the collected data, the resolution can be increased to a few nm. Due to the high resolution of these techniques even single molecules and their individual behaviour can be examined, which is not possible with conventional microscopes. 3D orbital tracking is a super resolution technique where the focus follows one particle in real time. The feedback mechanism uses an intensity distribution which is acquired with a rotating laser focus around the molecule. This method allows non-invasive experiments over several minutes with single molecules. These kinds of experiments have the advantage that the dynamics and behaviour of a single particle is examined without being averaged out like in ensemble experi-

ments. The high spatial resolution of this technique allows to extract several informations out of the trajectory like the diffusional behaviour, interactions with other biomolecules or the kinetics of reactions.

Aims of this thesis

The orbital tracking setup used in this thesis was build by Yoshihiko Katayama and Ondrej Burkacky. The software for the tracking was developed by Enrico Gratton. However the source code was never published and therefore no changes to the tracking algorithm could be applied. The first project of this thesis was to replace this program. The theory of tracking was examined and a tracking algorithm was developed. The implementation of this algorithm in simulations and the effect of different parameters is discussed in detail in the chapters *Orbital tracking* (p. 15) and in the subchapter *Simulations* (p. 25). Although the actual implementation of this algorithm on the new hardware was not achieved within this thesis, the program structure of the different components is explained in the subchapter *Hardware programming* (p. 34).
The second project of this thesis was to analyse and suppress the anisotropy of the setup's current configuration. A cage was constructed around the microscope to prevent the evaporation of the immersion water caused by the air conditioning and the ventilation system. The chapter *Isotropy of the Setup* (p. 37) shows the improvement to the mean square displacement calculations.

Chapter 1

State of the art

1.1 Fluorescence

Fluorescence describes the phenomenon of spontaneous emission of a photon from an excited molecule. This process can occur after the excitation with a shorter wavelength photon coming from a laser, arc lamp or just the sunlight. The term fluorescence was coined by the irish scientist Sir George Gabriel Stokes in 1852 [4]. He observed the conversion of ultra-violet into visible light when passing through fluorit.

Jablonski Diagram

The process of fluorescence and the related phosphorescence can be described with a Jablonski diagram (Fig. 1.1) [5].

In the first step, the electronic ground state of a molecule ($S0$) absorbs a photon (A) and the molecule is excited to the next electronic state ($S1$) to different vibrational levels (thin lines). Through internal conversion (IC), vibrational relaxation, the molecule decays into the vibrational ground state. On the first excited electronic state the molecule can emit photons through two different routes. The main process is fluorescence where the molecule decays to the electronic ground state ($S0$) within nanoseconds with the emission of a photon. The second process, phosphorescence, is the change from the singlet to the triplet state ($T1$) by intersystem crossing (ISC). In this process the spin is flipped. From the triplet state a photon can be emitted by another spin flip. Although this process is forbidden, it can still occur with a lower probability.

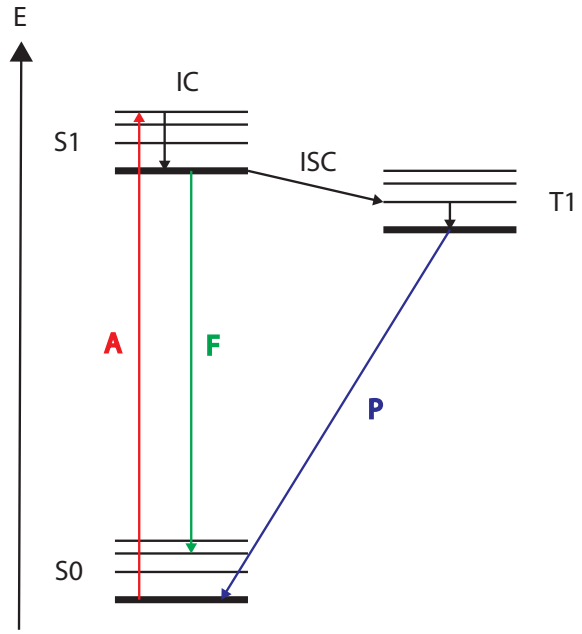

Figure 1.1: Jablonski diagram: absorption of a photon (A), fluorescence (F) and phosphorescence (P)

Absorption and emission spectrum

The absorption and emission spectrum of a fluorophore can be explained with the Franck-Condon principle of electronic transitions. The probability of a transition between two electronic states and their vibrational levels is given by the following equation:

$$P =< \Psi'|\mu|\Psi >= \int \Psi'^{*}\mu\Psi d\tau \tag{1.1}$$

where $\mu = \mu_e + \mu_N$ is the molecular dipole operator and Ψ is the product of the electronic, vibrational and spin wavefunctions $\Psi = \Psi_e\Psi_v\Psi_s$ the equation (1.1) can be written as

$$\begin{aligned} P = &\int \Psi'^{*}_v\Psi_v d\tau_n \int \Psi'^{*}_e\mu_e\Psi_e d\tau_e \int \Psi'^{*}_s\Psi'^{*}_s d\tau_s \\ &+ \int \Psi'^{*}_e\Psi_e d\tau_e \int \Psi'^{*}_v\mu_N\Psi_v d\tau_n \int \Psi'^{*}_s\Psi'^{*}_s d\tau_s \end{aligned} \tag{1.2}$$

Since electronic wavefunctions of different eletronical states or orthogonal, $\int \Psi'^{*}_e\Psi_e d\tau_e = 0$ and equation (1.2) reduces to

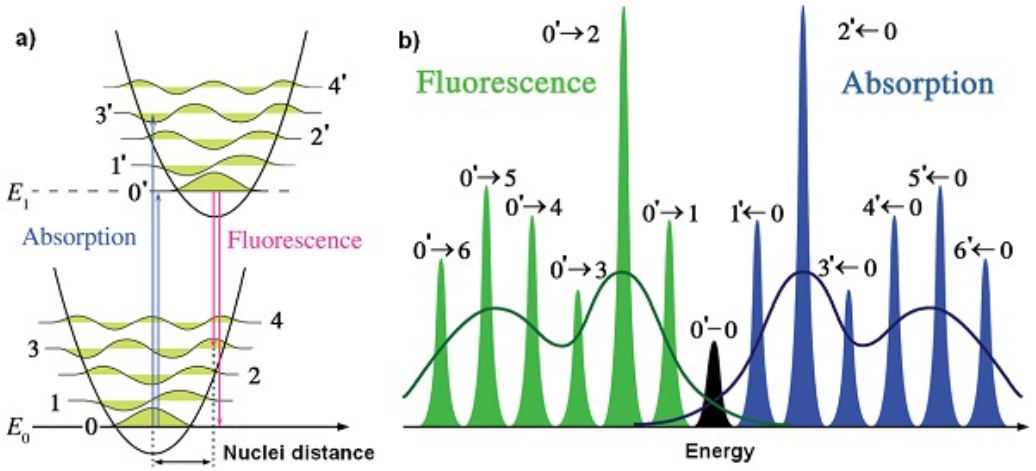

Figure 1.2: Schematic of the Franck-Condon principle (a) and the corresponding transitions in the absorption and emission spectrum (b) [6]

$$P = \int \Psi_v'^* \Psi_v d\tau_n \int \Psi_e'^* \mu_e \Psi_e d\tau_e \int \Psi_s'^* \Psi_s'^* d\tau_s \tag{1.3}$$

The probability density now is the product of the Franck-Condon factor $\int \Psi_v'^* \Psi_v d\tau_n$, the overlap integral between two vibrational states, the orbital selection rule $\int \Psi_e'^* \mu_e \Psi_e d\tau_e$ and the spin selection rule $\int \Psi_s'^* \Psi_s'^* d\tau_s$. For absorption and fluorescence the orbital and spin parts do not change for different vibrational transitions between two different electronic states and therefore the probability of absorption is approximately solely dependant on the Franck-Condon factor which is a function of the nuclear coordinates. The adsorption and emission now can be seen as the sum of broadened transitions between different vibrational levels. The amplitude of each transition is scaling with the corresponding Franck-Condon factor (Fig. 1.2). The energy loss during the internal conversion results in an energy shift between the adsorption and emission spectrum and is called Stokes Shift.

Fluorophores are usually excited with a laser, so only a narrow energy window is used to excite a molecule. Internal conversion occurs on a much faster timescale ($10^{-12}s$) than the fluorescence decay from the excited to the ground state ($10^{-9}s$). This means that only one wavelength of the absorption spectrum is needed to get the full emission spectrum (Kasha's rule).

Fluorescence lifetime and quantum yield

Two main properties of fluorophores are important for their use in experiments [5]. The first one, the fluorescence lifetime, is the average time the fluorophore stays in the S1 state. The lifetime is given by the fraction of one over the sum of all decay rates that lead out of the $S1$ state:

$$\tau = \frac{1}{\Gamma + k_{nr}} \tag{1.4}$$

where Γ denotes all radiative and k_{nr} all non-radiative processes. The natural or intrinsic lifetime in the absence of non-radiative processes is given by:

$$\tau_n = \frac{1}{\Gamma} \tag{1.5}$$

The second property that a fluorophore exhibits, the quantum yield, describes the ratio between absorbed and emitted photons:

$$Q = \frac{\Gamma}{\Gamma + k_{nr}} \tag{1.6}$$

The intensity of the fluorescence can be altered by several factors, this phenomenon is called quenching. Some of these mechanisms affect the excited state of the molecule, for example the Förster Resonance Energy Transfer, collisional quenching and excimer formation. These mechanisms are dynamic, an example for a static quenching mechanism is the formation of a dimer from two non excited molecules. The new molecule has a new adsorption and emission spectrum, quantum yield and lifetime.

1.2 Diffusion

In 1785, Jan Ingenhousz observed the motion of ash particles on alcohol [7]. In 1827, Robert Brown rediscovered this motion with pollen grains [8]. In 1905, Albert Einstein showed that the displacement of a free diffusing particle in n dimensions is given by [9]:

$$< \Delta R_x^2 >= 2nDt^{\alpha} \tag{1.7}$$

where <> denotes ensemble averaging, D the diffusion coefficient, t the time and $< \Delta R_x^2 >$ the mean squared displacement in the x direction. For Brownian motion, α equals 1. For a given trajectory, the mean squared displacement (MSD) is calculated with the following equation:

$$< \Delta R_{x,y,z}^2 >= \frac{1}{N-n} \sum_{t=1}^{N-n} (\vec{R}(t+n\Delta t) - \vec{R}(t))^2 \tag{1.8}$$

With increasing lag time $n\Delta t$ the number of available data points reduces $(N-n)$ and the uncertainty (calculated with the standard error of the mean) in the MSD points increases (Fig. 1.3). To obtain correct values of the diffusion coefficient only one quarter of the available MSD points should be used for a fit. Fig. 1.3 shows the MSD plot for 500 points of a simulated particle with Brownian motion (1000 data points). The first half of the MSD plot (blue) has enough data points to show the correct type of motion, Brownian movement. The statistics for the second half of the MSD plot (black) are not good enough and first the slope of the MSD decreases and in the end gets a negative sign, which does not depict Brownian motion.

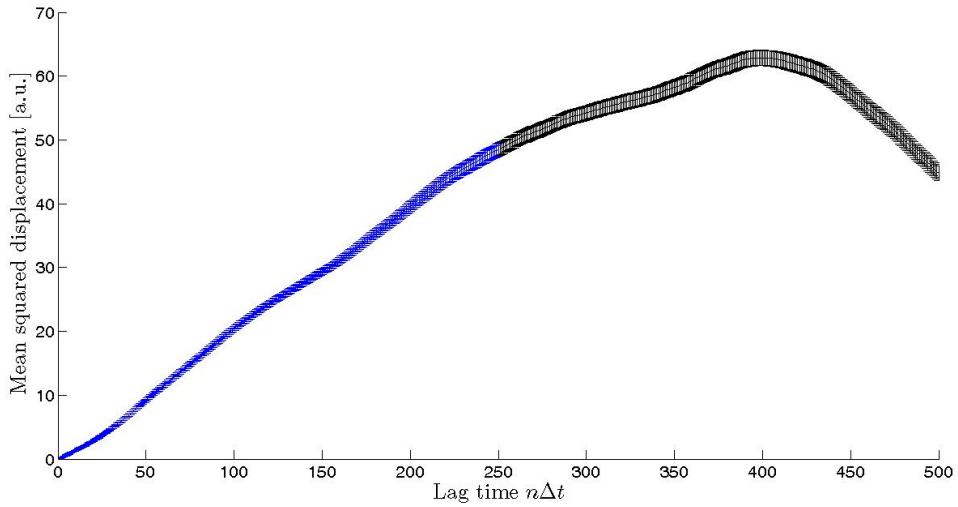

Figure 1.3: MSD plot of a simulated particle

However the environment in cells, networks or polymers differ completely. The motion in cells is influenced by active transport, cell compartments and interactions with the surrounding proteins, in networks or polymers the motion is hindered by the network structure. Active transport or anomalous diffusion result in either super-diffusive ($\alpha > 1$) or sub-diffusive ($\alpha < 1$) motion. Confined motion results in an asymptotic value for the mean squared displacement since the particle can not escape confinements of a defined size (Fig. 1.4). For confined motion, the Eq. (1.7) is modified to fit to the different behaviour of the particle:

$$< \Delta R^2_{x,y,z} >=< d_c^2 > [1 - A_1 e^{(-\frac{4A_2 Dn\Delta t)}{<d_c^2>})}] \tag{1.9}$$

$\sqrt{< d_c^2 >}$ is an approximation for the size of the compartment and A_1 and A_2 depict its geometry.

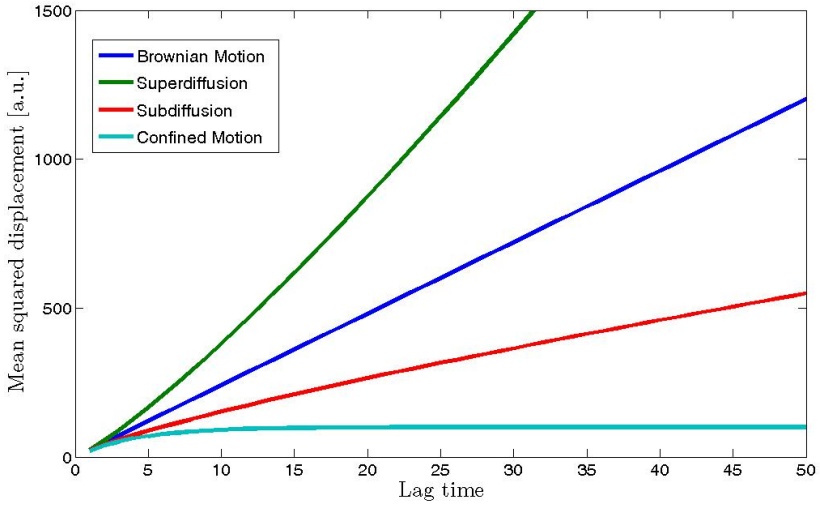

Figure 1.4: Diffusion types: Normal Brownian motion (blue, $\alpha = 1$), superdiffusion (green, $\alpha > 1$), subdiffusion (red, $\alpha < 1$) and confined motion (cyan)

1.3 Tracking Methods

The beginning of tracking experiments was a microscope which could follow living cells. Howard C. Berg developed this method in 1971 [10]. In 1991, Schätzel *et al.* described the first approach for single molecule tracking in 2D [11]. This approach used the back scattered light from latex particles to derive the position of the bead with a quadrant diode.They were able to track a bead on the millisecond time scale with a spatial resolution of 20 nm. Since this first approach more advanced tracking methods have been developed. The technical advances in the fields of photon detection, nanopositioning and most important the development of faster and cheaper computers have made it possible to track even single fluorophores in solution [12]. Today, there are two main approaches for single molecule tracking in 3D.

1.3.1 Analysis after acquisition

The first approach for 3D tracking is to separate analysis from image acquisition. The image is recorded and afterwards, the data is analysed with a fitting algorithm to subsequently extract the position. With this approach, multiple particles can be detected simultaneously but the detection volume is limited by the number of images in the Z direction and by the imaged area in the XY plane.

Z stacks

By collecting a number of 2D planes with different z positions with a wide-field, two-photon or confocal microscope, the 3D trajectory can be extracted (Fig.1.5). The resolution in time is limited by the speed of the image acquisition and the number of images per stack. A high distance between two images of a stack decreases the resolution in the Z direction and vice versa. The sampling rate used in modern microscopes for one image stack is ˜1 Hz [13].

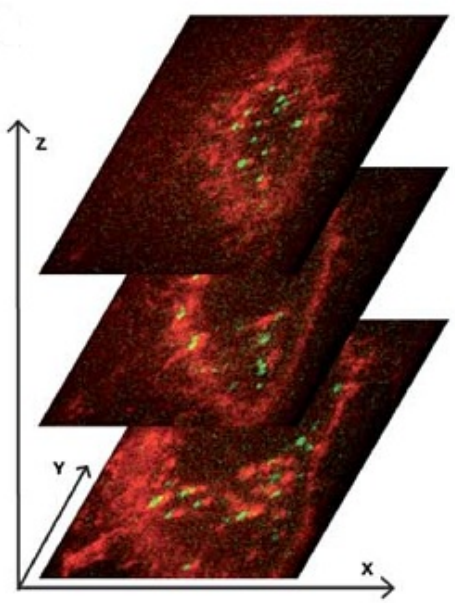

Figure 1.5: Image stack acquired with a spinning-disc confocal microscope [13]

Modification of the beam shape

To overcome the limitation of the time interval due to the z stacking, different groups introduced methods to alter the shape of the beam profile.
Kao and Verkman [14] used a cylindrical shaped lens in the detection path which resulted in an elliptical shape of the PSF below and above the focus whose orientation is shifted by 90° when passing through the focal plane (Fig. 1.6). The position in x and y was extracted from the centroid and the z position by the shape and orientation. They achieved a spatial resolution of 12 nm in z and 5 nm in the image plane. The maximum sampling rate was 250–330 ms per frame.

Off-focus mode

Speidel et al. [15] used the off-focus mode to extract the z-position by the shape and size of the off-focus pattern (Fig. 1.7). With increasing distance from the focal plane, the diameter of the PSF first increases and later intensity patterns are formed. The sub-nanometer resolution in the X,Y and Z directions was achieved only at a fixed position and got worse in all three axes with increasing distance from the focal plane. The sampling time was reduced by a factor of 10 to 106 ms.

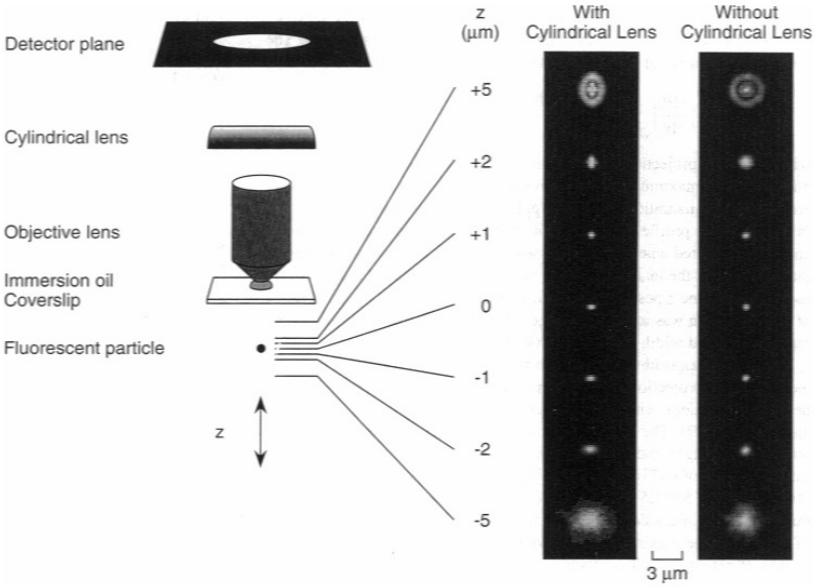

Figure 1.6: Effect of a cylindrical lens on the shape of the point spread function [14]

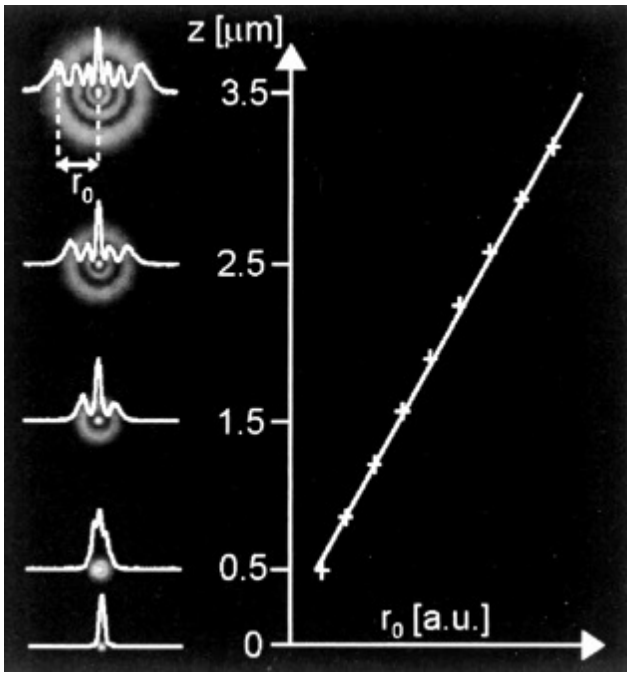

Figure 1.7: Off-focus tracking: Ratio between the outer ring of the PSF and the distance to the focal plane in off-focus mode [15]

1.3.2 Feedback approach

The second approach performs photon aquisition and analysis in real time. The position of the focus is changed constantly to follow the tracked particle. This approach needs fast calculations of the new position. The first microscope with nm resolution was developed in 1998 by Peters et al. [16]. In this setup, an analogue feedback system was used. Ten years later, more powerful computers and field programmable gate arrays (FPGA) are commercially available which can be used for more sophisticated tracking methods with faster sampling rates up to several kHz.

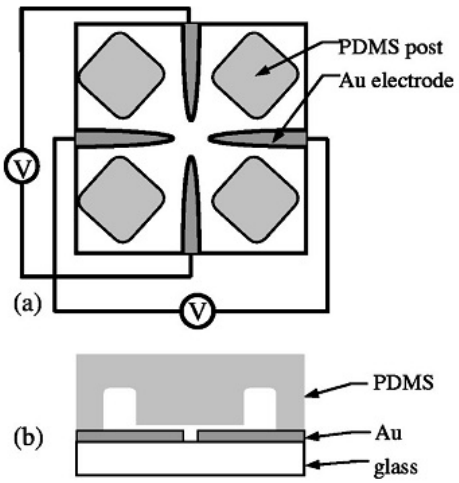

Figure 1.8: Schematic of the ABEL trap, front (a) and side view (b) [17]

ABEL trap

In 2005, Cohen and Moerner developed the Anti-Brownian Eletrophoretic Trap (ABEL) [17]. The sample holder of the ABEL trap is shown in Fig. 1.8. Z confinement is achieved by four polydimethylsiloxane (PDMS) posts and a second glass layer. The position of the particle is monitored by a CCD camera and processed by a normal computer. By applying a voltage in the X and Y directions a neutral particle is moved through electro osmotic flow or a charged one through electrophoresis and its brownian movement is cancelled out. The displacement trajectory from this method can be used as a pseudo free trajectory to calculate diffusion coefficients.

Tetrahedral detection

In 2007, Lessard et al. presented a tetrahedral detection approach (Fig. 1.9), which used 4 confocal detection volumes aligned along X and Y and shifted by an offset in Z [18].

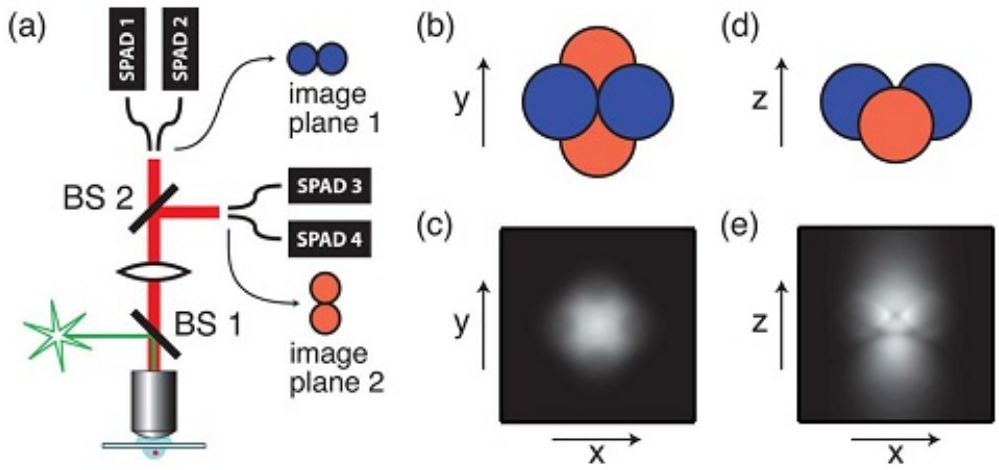

Figure 1.9: (a) Experimental setup. Alignment of the detection volumes in xy (b,c) and in xz (d,e). [18]

The modulation between two detection volumes in X and Y and by the two planes in Z is given by the following equation:

$$MOD = \frac{I_2 - I_1}{I_2 + I_1} \tag{1.10}$$

Where I_1 and I_2 are the intensities of the detector pair in X or Y direction of the corresponding axis. For the Z modulation I_1 and I_2 are given by the sum of the detectors in X and Y direction (Fig. 1.9). Once the modulation is calibrated, a look up table or an analytical function can be used to calculate the position out of the modulation. This method achieved a sampling rate of 5 ms with a spatial resolution of 95 nm.

Chapter 2

Orbital Tracking

The theory of the tracking method used in this thesis was first published by Jörg Enderlein in 2000 [19]. He proposed to rotate the laser beam around the particle and calculate the new XY position from the intensity distribution within one period. The Z position is encoded in the intensity ratio between two detection planes above and below the focal plane. Enrico Gratton built the first setup using this idea in 2004 [20]

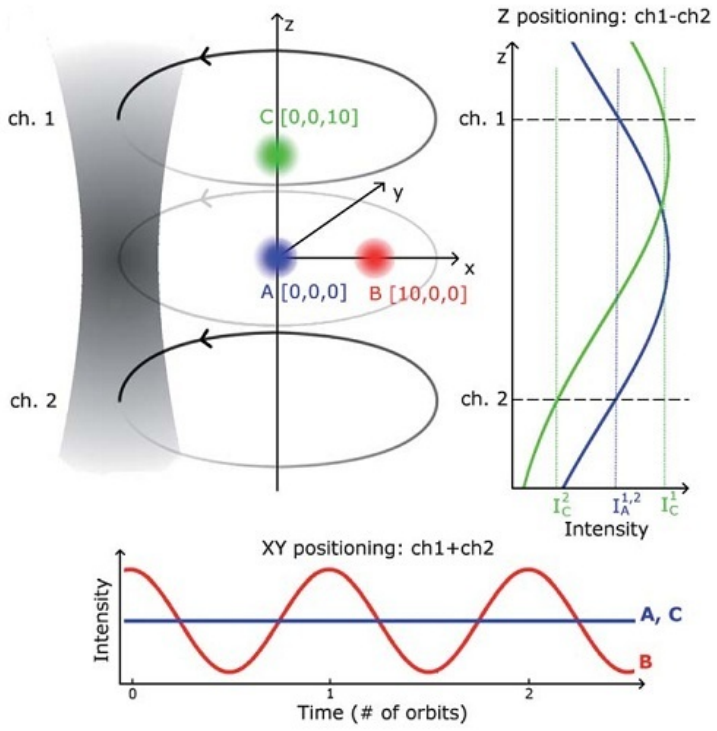

Figure 2.1: Orbit and Z intensities for different particle positions [13]

The XY position of the particle is encoded in the phase and modulation of the signal. Fig. 2.2 shows the intensity orbits for different angular positions of the particle. The maximum of the intensity orbit has the same angular position as the particle. Fig. 2.3 shows the intensity orbit for particles with varying distance to the scanner center. With increasing distance to the center the intensity of the particle first increases until it passes the scanning radius and then decreases. By combining the information out of the modulation and phase of the orbit, the exact position of the fluorophore in the XY plane can be determined (r, φ).
The calculation of the z position of the particle is done through two slightly shifted detection planes above and below the focal plane with two avalanche photo diodes. The exact position can be extracted from the intensity ratio between the two orbits. Fig. 2.4 shows the intensity of one particle for the two detection planes. Depending on the position, the ratio is negative, positive or zero for a fluorophore in the middle of the two planes.

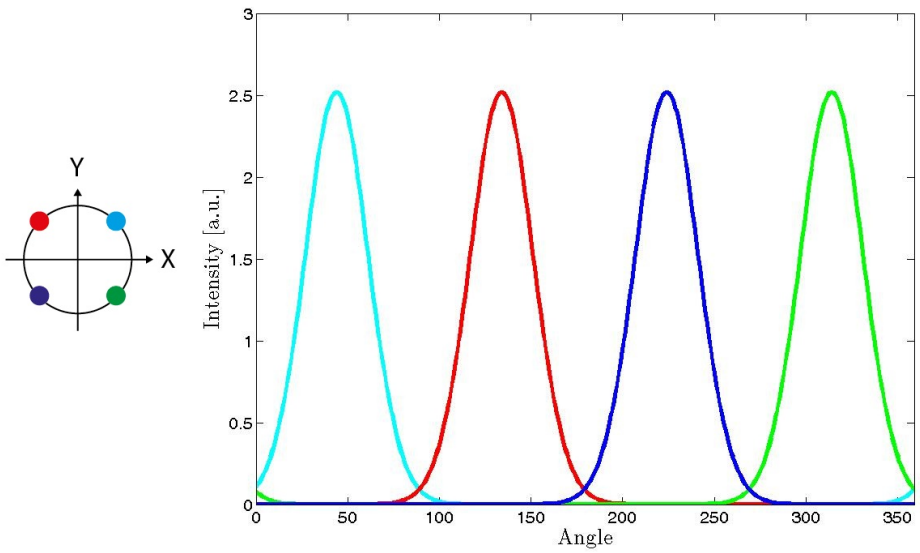

Figure 2.2: Simulated intensity of a particle with a fixed distance and a varying angle over one orbit

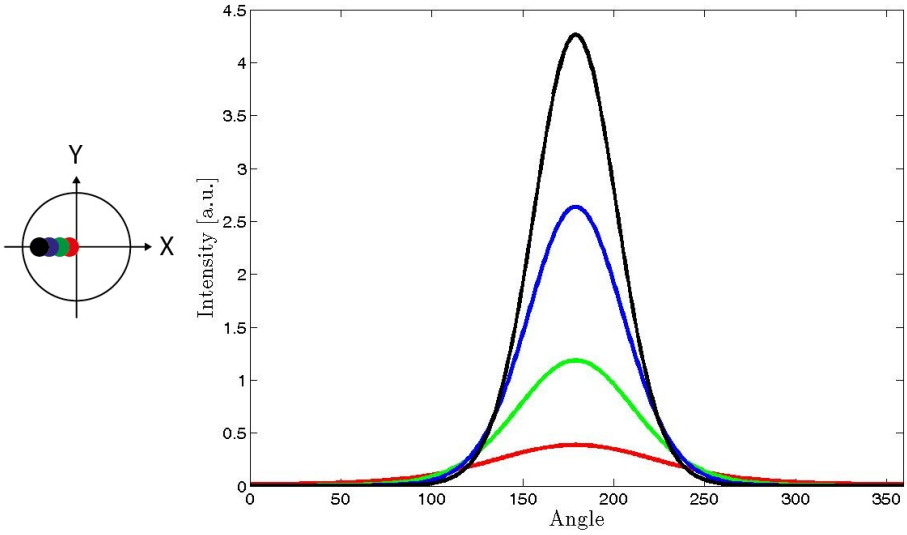

Figure 2.3: Simulated intensity of a particle with a fixed angle and a varying distance to the center of the scanning radius over one orbit

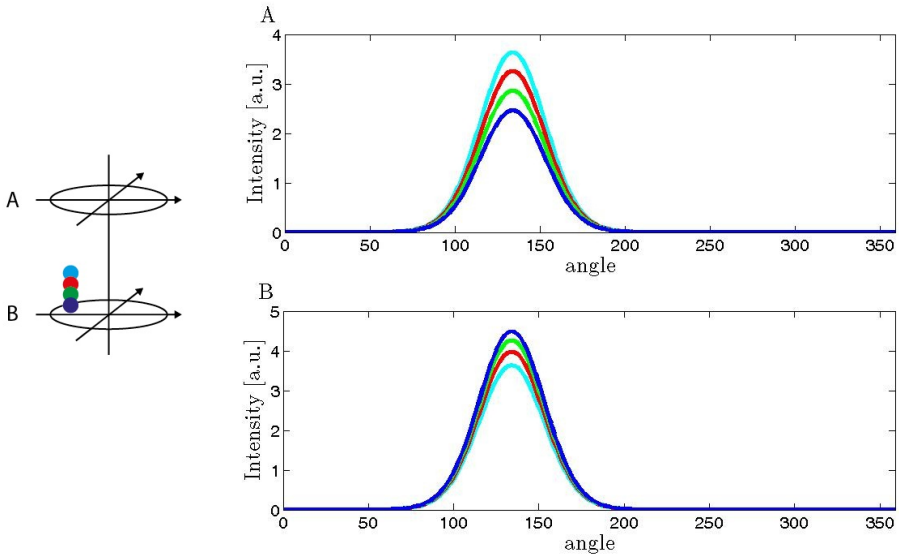

Figure 2.4: Simulated intensity of different particle positions for the two detection planes shifted by + (A) and - dz (B)

2.1 Theory

XY positioning

The periodic intensity signal $I(\varphi, r)$ as a function of the phase angle φ and the distance to the scanner position r can be described by the Fourier series with Eq. (2.1):

$$I(\varphi, r) = \frac{a_0(r)}{2} + \sum_{k=1}^{n} (a_k(r)\cos(k(\varphi)) + b_k(r)\sin(k(\varphi))) \tag{2.1}$$

where φ is the phase and a_k and b_k are the fourier coefficients. For the tracking algorithm it is more suitable to use the modulation and phase notation for the Fourier series (Eq. (2.2)):

$$I(\varphi, r) = \frac{a_0(r)}{2} + \sum_{k=1}^{n} (A_k(r)\cos(k(\varphi - \varphi_k))) \tag{2.2}$$

with

$$Mod(r) = A_k(r) = \sqrt{a_k(r)^2 + b_k(r)^2} \qquad and \qquad \varphi_k = \arctan\left(\frac{b_k(r)}{a_k(r)}\right) \tag{2.3}$$

In this notation A_1 corresponds directly to the distance to the center of the orbit and φ_1 to the angle(Fig. 2.5):

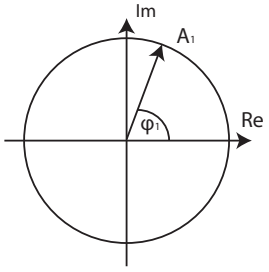

Figure 2.5: Modulation and phase in the complex plane

The coefficients a_1 and b_1 can be calculated by Eq. 2.4 and 2.5:

$$a_1(r) = \frac{1}{\pi} \int_{-\pi}^{\pi} I(\varphi, r)\cos(\varphi - \varphi_0) \quad d\varphi \tag{2.4}$$

$$b_1(r) = \frac{1}{\pi} \int_{-\pi}^{\pi} I(\varphi, r) \sin(\varphi - \varphi_0) \quad d\varphi \tag{2.5}$$

Where φ_0 is a phase shift of the sine and cosine functions. For the hardware implementation of the algorithm one needs two more additional components. The first one is the dependence of the modulation on the brightness of the tracked particle. To be independent from the intensity, the modulation is divided by $0.5 \cdot a_0(r)$ which is the average intensity:

$$a_0(r) = \frac{1}{\pi} \int_{-\pi}^{\pi} I(\varphi, r) d\varphi \qquad Mod(r) = \frac{\sqrt{a_1(r)^2 + b_1(r)^2}}{0.5 a_0(r)} \tag{2.6}$$

With this modification a calibrated look-up table for the modulation can be used for the distance calculation. The second modification is caused by a phase change, the physical angle. Due to the geometry of the setup, the pattern shown it Fig. 2.5 may be shifted by an angle φ_0:

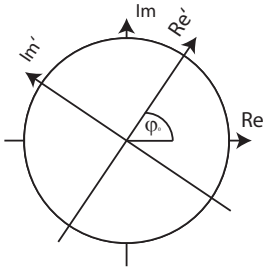

Figure 2.6: Difference between the theoretical axis position (Re and Im) and the actual situation in the setup (Re' and Im')

There are two possible options to counteract this effect. The first option is to adjust φ_o in the calculation of the $a_1(r)$ and $b_1(r)$ coefficients in Eq. (2.4) and (2.5). The second option is to introduce the phase shift directly in the sine and cosine waves for X and Y in the scanning orbit:

$$V_X(\varphi) = A_X \sin(\varphi + \varphi_0) + V_{X0} \quad and \quad V_Y(\varphi) = A_Y \cos(\varphi + \varphi_0) + V_{Y0} \tag{2.7}$$

where V_X and V_Y are the voltage inputs for the two axes, A_X and A_Y for the radius size and V_{X0} and V_{Y0} as offset voltages for the position of the orbit.

Z positioning

The intensity variation between the two detection planes is used to calculate the Z position:

$$Mod(z) = \frac{a_0(r,1) - a_0(r,2)}{a_0(r,1) + a_0(r,2)} \tag{2.8}$$

where $a_0(r,1)$ and $a_0(r,2)$ are the zero order terms of the cosine series for the two detection planes. The calculation of the Z position is also done with a calibrated look-up table.

The theory as described in this chapter was used during the thesis to develop program structures for the orbital tracking confocal microscope and simulations to examine the behaviour of the algorithm.

2.2 Orbital Tracking Setup

2.2.1 Current configuration

Hardware

The figure 2.7 shows the tracking setup in the current configuration. Three lasers (488, 561 and 633 nm) are coupled via dichroic mirrors (D1-3, AHF Analysentechnik) into a single mode fiber (AMS Technologies). The gaussian-shaped beam is collimated after the fiber and is directed via a silver mirror (M2, AHF Analysentechnik) and a dichroic mirror (D4, AHF Analysentechnik) onto the XY piezo-mirror (Physik Instrumente). The mirror plane is imaged by two lenses onto the back aperture of the objective (Nikon 60x/1.2) which focuses the light onto the sample. The fluorescence is guided back over the tilting mirror and passes the dichroic mirror (D4), which also cuts off backscattered light from all three lasers. A 50/50 beamsplitter (AHF) divides the fluorescence, which is focused with two lenses onto two fiber coupled avalanche photo diodes (APD, Perkin Elmer). The entrance of the fiber acts as a confocal pinhole and cuts off out-of-focus light. The TTL pulses from the two APDs are gathered with the ISS FCS Card.

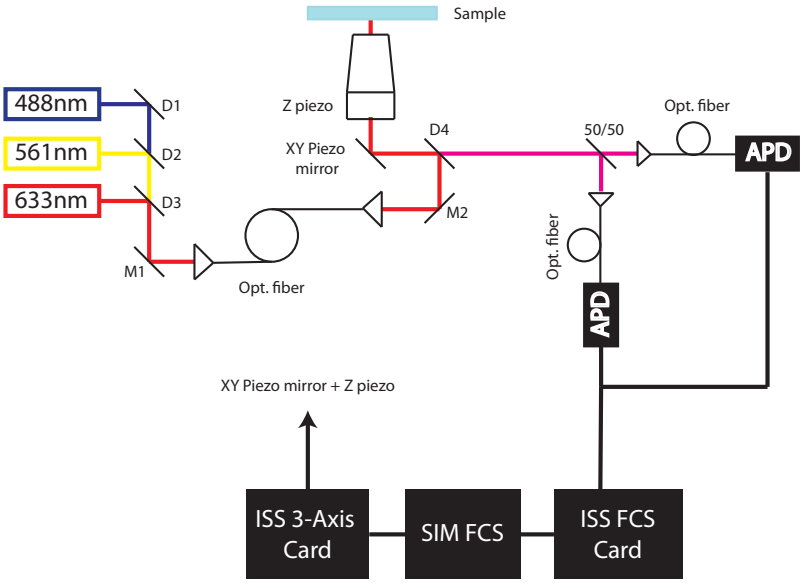

Figure 2.7: Schematic of the tracking setup

For the analysis and position calculation a program written by Enrico Gratton is used (SIM FCS). A 3-Axis card (ISS) controls the positioning

of the tilting mirror in the XY plane and the objective piezo the position in the Z direction. The additional widefield path is not displayed. The combination of the widefield detection with the orbital tracking allows to examine the interactions of the particle with the cell environment. This combination overcomes the main disadvantage of the orbital tracking, to be blind to the particle's surroundings.

Accuracy

The accuracy of the setup in the X,Y and Z direction was measured with a fixed and a moving fluorescent bead. The movement of the particle was introduced with a piezo stage on top of the microscope. The accuracy for the fixed particle was calculated with the standard deviation of the position. To determine the dynamic accuracy, the bead was displaced with sine motions in all 3 dimensions (Fig 2.8). Since the amplitude and frequency of the movement are known, the trace could be fitted and the standard deviation of the residues was calculated. Table 2.1 shows the accuracy of the current configuration for a particular track. The accuracies in X and Y directions have similar values but differ much from the accuracy in z direction which is consistent with the theory of the tracking algorithm.

Table 2.1: Fixed and dynamic accuracy of the setup

	X	Y	Z
Fixed $[nm]$	9.11	11.17	21.27
Dynamic $[nm]$	8.91	11.28	20.87

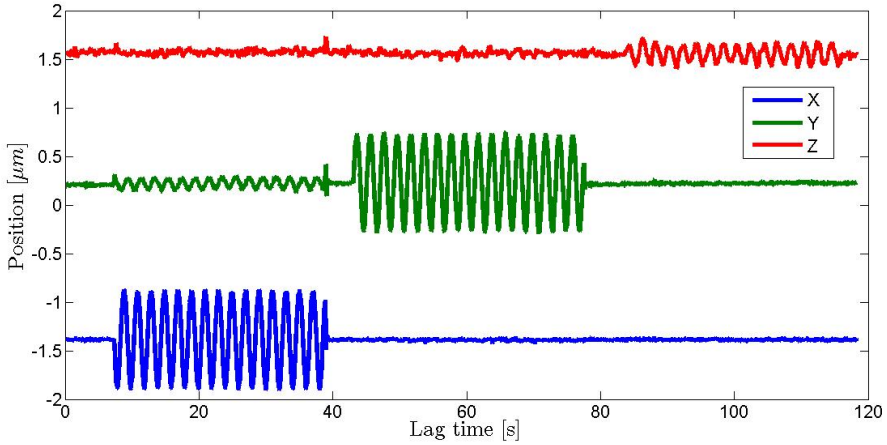

Figure 2.8: Fixed particle on an oscillating piezo stage

2.2.2 Hardware upgrades

The current configuration does not allow changes in the experimental parameters because of the non-public source code. To overcome this issue the ISS cards and the computer will be replaced by a field programmable gate array (FPGA). The National Instruments cRIO 9076 reconfigurable I/O system provides a real-time CPU, a field programmable gate array and replaceable modules for digital and analogue I/O. This system allows a lag-free and parralel calculation of the position with faster timing than reported previously by Y. Katayama [21]. This hardware allows the separation of the positioning algorithm and the data recording from the windows operating system which is not suitable for accurate high speed applications. The program flow is explained in more details in the chapter *Programming*. Due to the high delay time of the piezo mirror compared to galvano positioning systems, galvano mirrors could provide a faster scanning and orbit speed which would improve the resolution in time. Therefore fluorophores with a higher diffusion coefficient can still be tracked. The current positioning program (SIM FCS) does not allow particle tracking outside a volume of 20x20x10μm. For biological applications, for example tracking in zebrafish embryos, the distance in the X and Y directions should be in the order of mm and in the Z direction in the order of 100 μm. This detection volume can be achieved by a new tracking program, which does not limit the XY mirror and the Z piezo positioner and the coupling to an additional positioning stage on top of the microscope.

Chapter 3

Implementation of the tracking algorithm

3.1 Simulations

To study the influence of different parameters on the tracking accuracy two programs simulating Brownian motion and the tracking algorithm were created. The programs were written for Matlab R2011b and LABVIEW.

3.1.1 Simulation algorithm

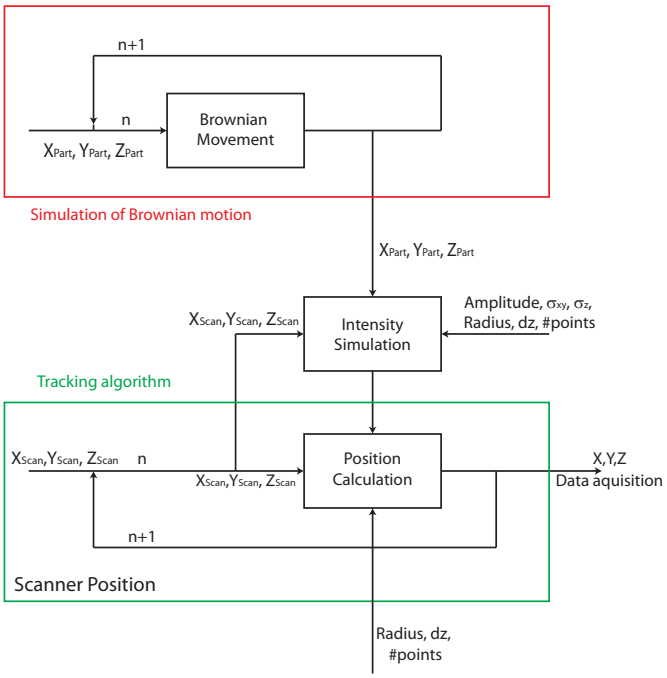

Figure 3.1: Program flow for the simulation programs

Both programs use the same program flow for the simulations (Fig. 3.1). The Brownian motion (red) is calculated independently for each axis and updates the position $(X_{Part}, Y_{Part}, Z_{Part})$ for every iteration. The position of the particle is then handed over to the Intensity algorithm. This algorithm uses the amplitude, the width of the point-spread function (PSF) (σ_{XY}, σ_Z), the scanning radius in the XY plane (Radius), the distance between the focal and detection planes in the z direction (dz), the number of points in the orbit (# points) and the position of the scanner $(X_{Scan}, Y_{Scan}, Z_{Scan})$ to calculate the intensity orbits. The calculation of the new position (green) is also done for every iteration. The positioning algorithm uses the two intensity orbits, the current scanner position, the scanning radius, the distance between the two detection planes and the number of orbit points to calculate the position of the particle in relation to the scanner. The scanner position is updated for the next iteration and the position is logged in a text file.

Brownian motion

The Brownian motion was programmed using a normal distribution with the implemented random generators of Matlab and Labview. The value for each step was calculated separately in the X,Y and Z directions.

Intensity Simulation

The intensity orbits of the detection planes were simulated with a 3D Gaussian:

$$I(r,\varphi,dz) = A_0 \cdot e^{-0.5\cdot\left(\left(\frac{X-X_0}{\sigma_{xy}}\right)^2+\left(\frac{Y-Y_0}{\sigma_{xy}}\right)^2+\left(\frac{Z_0\pm dz}{\sigma_z}\right)^2\right)} \tag{3.1}$$

where dz is the distance between focal and detection planes, A_0 the amplitude, σ_{xy} and σ_z the widths of the PSF in the X,Y and Z directions and X_0,Y_0 and Z_0 the differences between scanner and particle positions. X and Y were calculated with a specific number of points (# points) by the following equations to generate the scanning orbit:

$$X(n) = R_{Scan}\cdot\cos\left(2\pi\frac{n}{\#points}\right) \qquad Y(n) = R_{Scan}\cdot\sin\left(2\pi\frac{n}{\#points}\right) \tag{3.2}$$

Position calculation

For the calculation of the new position, calibrated look-up tables(LUT) are used since the calculation of the correct analytical equation is too slow. These LUTs are highly dependent on the tracking ratios $\frac{R_{Scan}}{\sigma_{XY}}$ in XY and $\frac{dz}{\sigma_Z}$ in Z. Fig. 3.2 and 3.3 show different ratios for the look-up tables in XY and Z. For the following simulations a ratio of 1:1 for the XY plane and a ratio of 1:4 for the Z direction were chosen.
In this algorithm the XY plane is decoupled from the Z axis. For a constant Z term, the 3D Gaussian simplifies to a 2D Gaussian and inversely for constant X and Y to a 1D Gaussian:

$$I(r,\varphi) = A_0 \cdot e^{-0.5\cdot((\frac{X-X_0}{\sigma_{xy}})^2+(\frac{Y-Y_0}{\sigma_{xy}})^2}\cdot A_z \tag{3.3}$$

and

$$I(dz) = A_0 \cdot e^{-0.5\cdot((\frac{Z_0\pm dz}{\sigma_z})^2)}\cdot A_{x,y} \tag{3.4}$$

For a constant position of the two detection planes the modulation in the Z direction remains constant for varying X and Y positions (Eq. (2.8)).

The modulation in the XY plane shows the same behaviour for varying Z positions (Eq. (2.3)). Therefore the XY plane and the Z axis are decoupled.

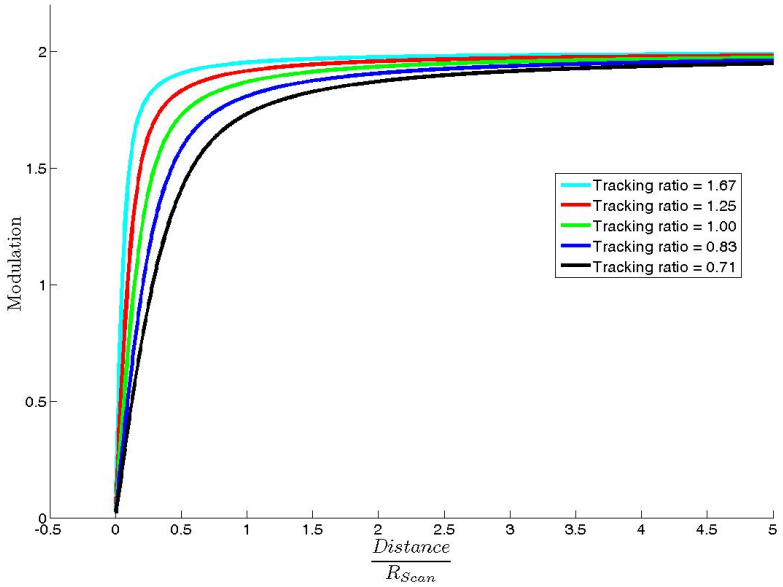

Figure 3.2: XY Modulation for different tracking ratios

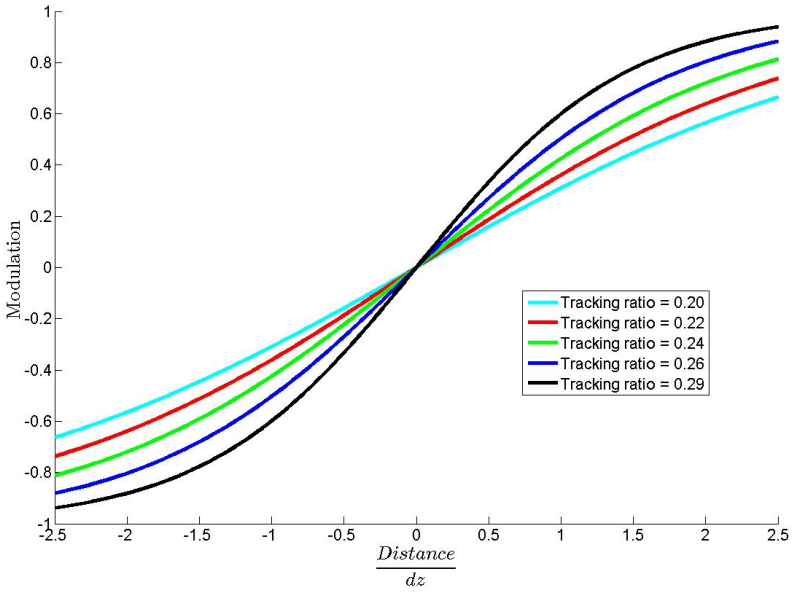

Figure 3.3: Z Modulation for different tracking ratios

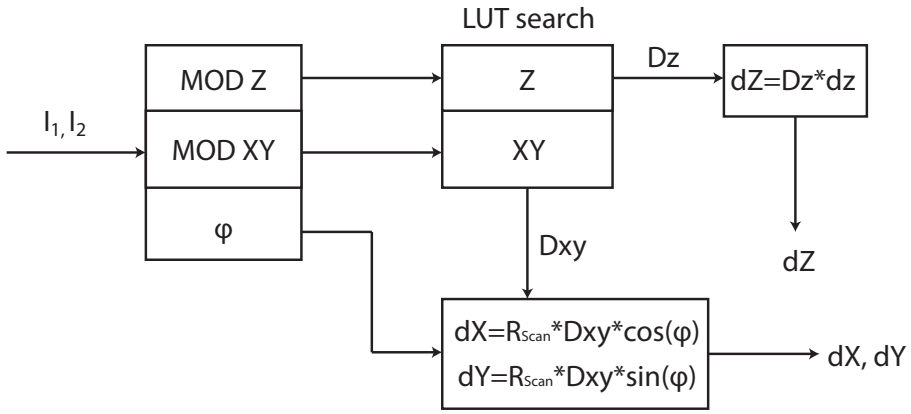

Figure 3.4: Flowchart of the positioning algorithm

Fig. 3.4 shows the positioning algorithm. The intensities of the two detection planes (I_1 and I_2) are used to calculate the modulation for XY and Z as well as the angle φ with equations (2.3) , (2.6) and (2.8). In the next step the two LUTs for XY and Z are searched for the modulation values and the corresponding distances (Dxy and Dz). The final step is the calculation of the displacements in the X,Y and Z directions (dX, dY and dZ).

3.1.2 Influence of the scanning parameters

The tracking algorithm has 3 parameters which can be changed, number of points in the orbit and the two tracking ratios for XY and Z. The effects of these parameters on the tracking error and on the MSD plots of a 100,000 cycles track are examined in this chapter.
The error in two dimensions is calculated with Eq.(3.5) where Δx and Δy denote the difference between scanner and particle position in the X and Y directions and $< dR >$ is the mean distance between two positions of a particle.

$$Tracking \quad error = \frac{\sqrt{\Delta x^2 + \Delta y^2}}{< dR >} \tag{3.5}$$

The effect on MSD plots is calculated with the error of the scanner MSD plot (Eq. (3.6)) relative to the simulated particle's MSD.

$$MSD_{error(i)} = \frac{MSD_{Scanner(i)} - MSD_{Particle(i)}}{MSD_{Particle(i)}} \tag{3.6}$$

Number of points in the orbit

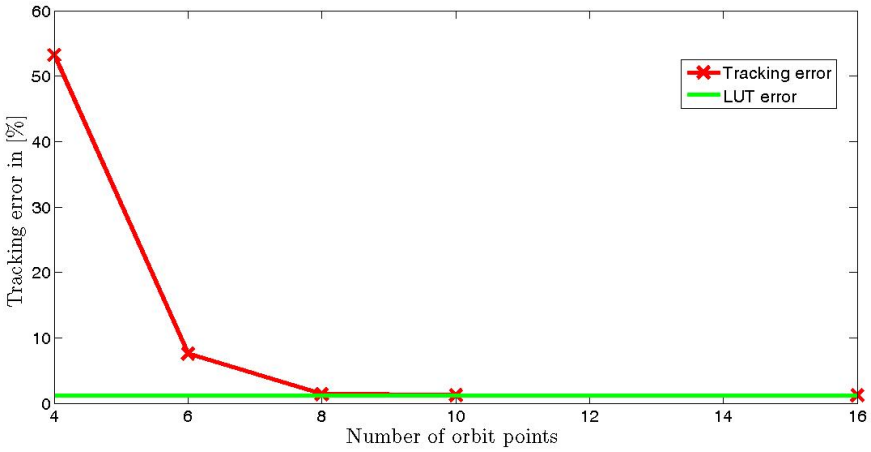

Figure 3.5: Tracking error for different number of orbit points

Fig. 3.5 shows the tracking error for different numbers of orbit points. The smallest possible tracking error can be calculated by dividing the distance between two points in the LUT by two (LUT error). The trajectory of the

scanner position with only four points shows that the algorithm gets unstable, because not enough points are used for the calculation of the coefficients. After 10 points the tracking error is already at the minimum and therefore it is sufficient to use 10 or 16 points per orbit which speeds up the position calculation.

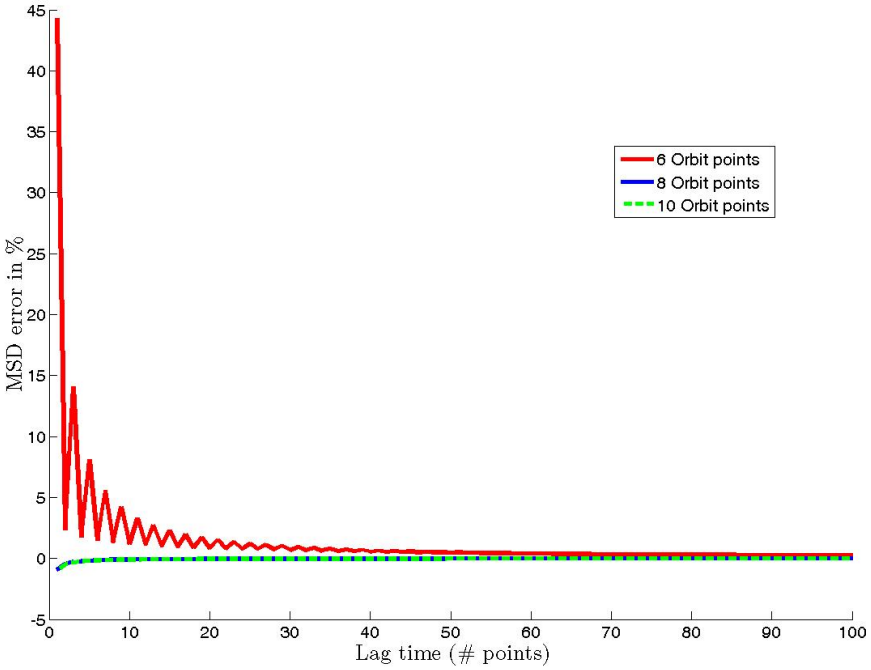

Figure 3.6: MSD error for different number of orbit points

Fig. 3.6 shows the error between scanner and particle MSDs for 6, 8 and 10 orbit points. As expected, the error for 6 points has the biggest value and converges to a value close to zero with increasing lag time. The error for 8 and 16 points shows the same behaviour. The slight decrease at the beginning of the MSD plots with 8 and 10 points is introduced by the LUT (LUT error).

Wrong look-up tables

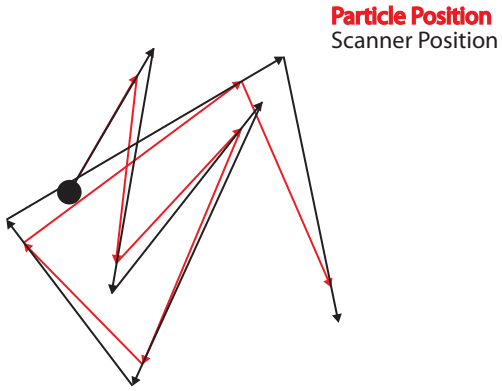

Figure 3.7: Scanner position in 2 dimensions in relation to the particle position for a tracking ratio greater 1

In reality the size and therefore the point spread function of a molecule is not always known. This means that the tracking ratios used for the calculation of the LUT differ from reality. Depending on the LUT the scanner travels too far for tracking ratios bigger than 1 or too short for values smaller than 1 in comparison to the actual particle position in the XY plane (Fig. 3.7). The same behaviour can be observed for the Z direction.

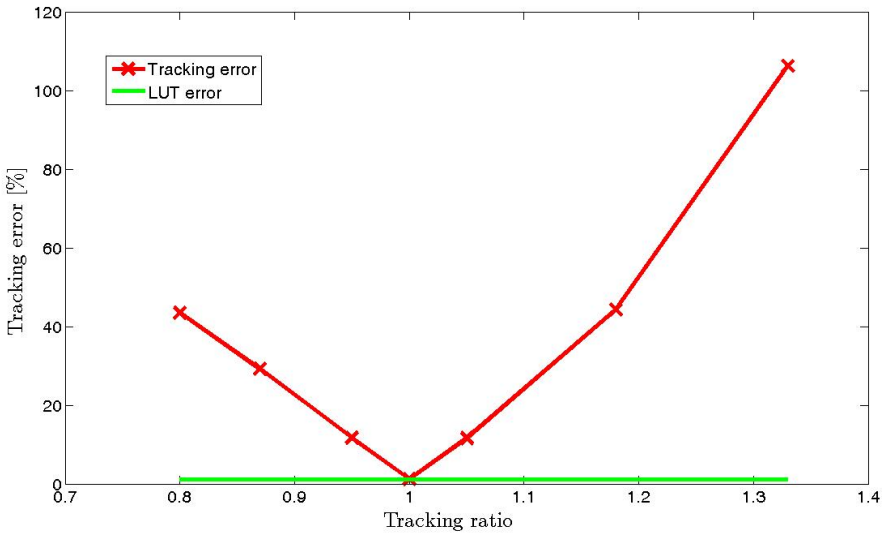

Figure 3.8: Tracking error for different XY tracking ratios

Fig. 3.8 shows the tracking error for different tracking ratios. A 5% change in the tracking ratio increases the error by approximately 10%. The MSD error for all ratios of Fig. 3.8 is shown in Fig. 3.9. The error between the scanner and particle MSDs is converging to zero for all ratios. The behaviour of the MSD errors is dependant on the magnitude of the tracking error. For big tracking errors, the MSD error is converging more slowly and from a higher starting point.

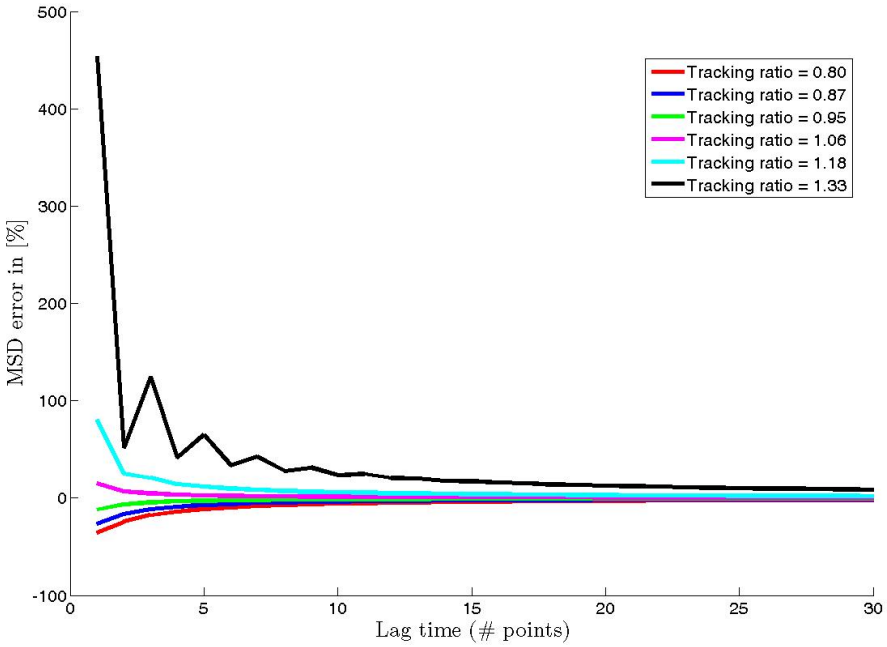

Figure 3.9: MSD errors for all tracking ratios of Fig. 3.8

Table 3.1 shows that the influence of the error on the MSD fit. As expected, when more points of the first quarter of the MSD are used, the influence of the error on the diffusion coefficient and the α value decreases.

The simulations presented in this chapter to examine the behaviour of the tracking algorithm can be used to optimize the tracking algorithm. Not only the importance of correct tracking ratios which differ for different wavelengths was revealed, but also the minimum number of orbit points, which are necessary for tracking. When using this tracking algorithm, one has to pay attention for the first 20-30 points in the MSD (Fig. 3.9). This critical part reveals if the tracking ratio was adjusted properly or still has to be optimized. The considerations for a wrong LUT for the XY positioning can also be applied for the Z positioning. The two errors for the XY plane and

Table 3.1: Fitted diffusion coefficients and α exponents for different number of MSD points

	Particle	Scanner
D [a.u.] 50 points	1.21	0.88
D [a.u.] 100 points	1.21	0.95
D [a.u.] 200 points	1.22	1.03
D [a.u.] 400 points	1.18	1.01
α 50 points	1.00	1.09
α 100 points	1.00	1.05
α 200 points	1.00	1.03
α 400 points	1.00	1.02

the Z axis may compensate each other or add up in the 3D MSD, depending on the tracking ratios in XY and Z.

3.2 Program flow for the new hardware

The first consideration for the programming of the National Instruments FPGA is to distinguish between tracking and positioning accuracy. The positioning accuracy is a fixed value given by the precision of the tilting mirror. The tracking accuracy is the resolution of the tracking algorithm and is determined by the number of photons and the accuracy of the LUT when no other errors are present. Since the position of the particle is always calculated with respect to the scanner position, the positioning resolution should be smaller than the full width at half maximum (FWHM) of the particle's PSF. After each cycle the scanner is moved to the position with the smallest distance to the particle (Fig. 3.10).

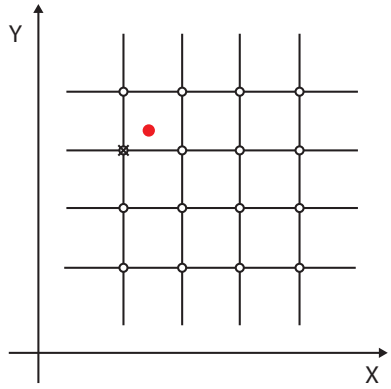

Figure 3.10: Possible scanner positions (black circles), a particle (red) and the optimal scanner position (cross)

Therefore the programming can be divided into two parts with different data types. The FPGA platform has two parts which can be programmed independently. The first part is an industrial real time CPU for data logging and analysis which can handle floating point data types. The second part is the LX45 FPGA which is used for data acquisition and the controlling of the tilting mirror and the objective piezopositioner. However the FPGA module can only handle a less powerful implementation of decimal digits, the Fixed Point data type with a grid size which has to be previously defined. Therefore the whole tracking program is divided between the real time controller, the LX45 FPGA and the host computer (Fig. 3.11).

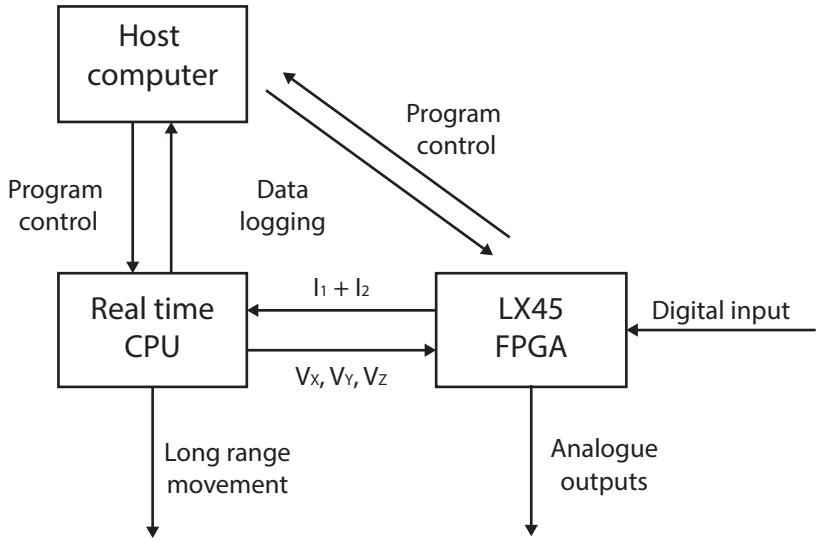

Figure 3.11: Hardware communication and program flow

LX45 FPGA

The FPGA is used to control the analogue outputs for the tilting mirror and the z objective piezo positioner and the digital input for the acquisition of TTL pulses from the two avalanche photo diodes. The position of the scanning image and the orbit is given by the offset value in X,Y and Z direction (V_X,V_Y and V_Z) and is calculated with the tracking algorithm on the real time CPU. The waveforms used for the creation of the scanning image and the orbit are stored on the FPGA in the memory and read out point by point for the corresponding focus position. For the timing of the photon acquisition, the internal clock of the FPGA is used. The data is

transferred to the real time CPU with first in first out buffers (FIFO).

Real time CPU

On the real time CPU, the tracking algorithm presented in figure 3.4 reads out the intensity orbits of the FPGA and calculates the exact position of the particle with a floating point data type. This ensures enough decimal digits to achieve the accuracy of the LUT. The new position is sent back to the LX45 FPGA with a grid size of the fixed point data type which matches the positioning accuracy of the scanner. The position and intensity data is collected and after the track is finished, transferred to the host pc. For the long range tracking which was mentioned before, the real time computer can control a microscopy stage with a stepper motor via a RS232 port.

Host computer

The host computer controls the different functionalities of the hardware and is used for the data storage after each track. No time critical calculation is run on the host computer since a tracking program on windows can interfere with other software, which can result in loss of data as described before [21].

Chapter 4

Isotropy of the setup

The orbital tracking setup used in this thesis can introduce an anisotropy to the tracked particle because of drift. The influence of this effect is analysed with a 2D mean square displacement for the xy, the xz and the yz planes. The calculation was done with Eq. (1.8) which was reduced for two dimensions.

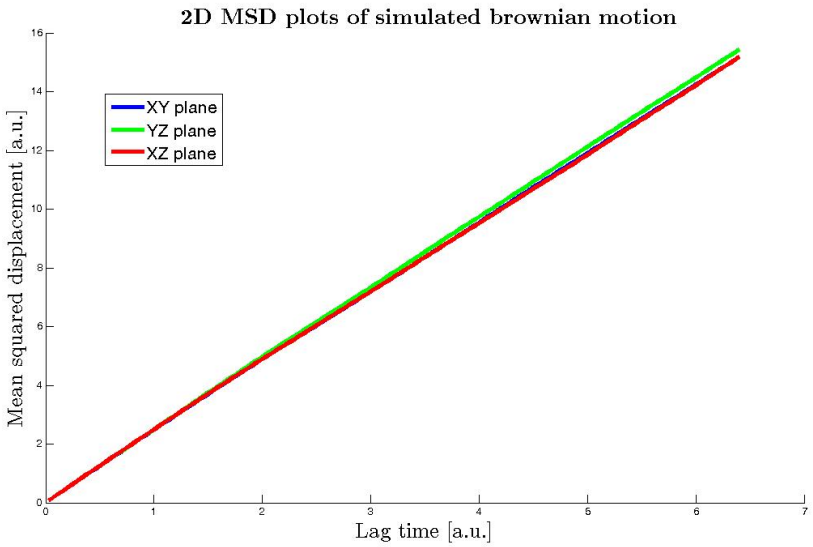

Figure 4.1: 2D MSD plots of pure Brownian motion of the XY,YZ and XZ plane

Fig. 4.1 shows that the three MSD plots of simulated data (100,000 points) for the 2D planes are almost identical. As expected no anisotropy is visible and the diffusion coefficients D and α values are also almost identical. However, the orbital tracking setup did show a complete different behaviour. Fig. 4.2 shows the 2D MSD plots for $200nm$ fluorescent beads (Spherotech Rainbow) in a glycerol water (60:40 v/v) mixture. The MSD plots for the

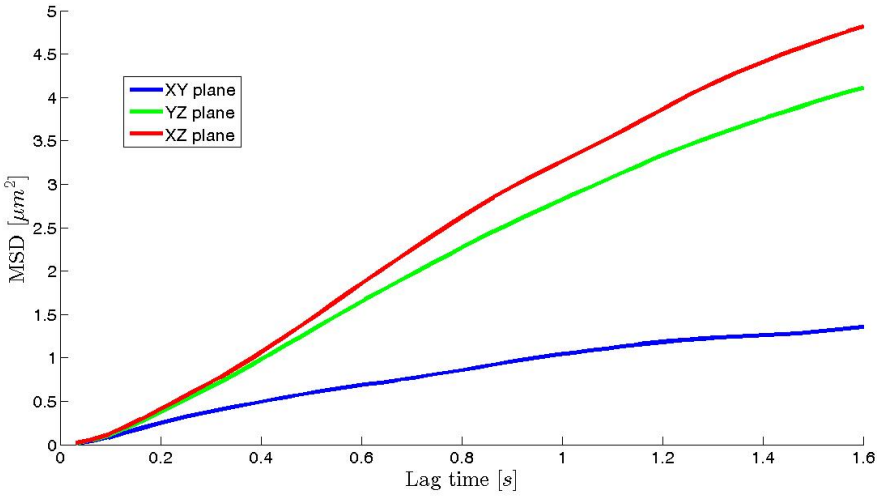

Figure 4.2: 2D MSD plots of fluorescent beads in a glycerol water mixture (60/40 v/v).

YZ and XZ planes are similar but do not show a Brownian behaviour. The MSD plot for the XY plane differs completely from the two other planes and also shows no pure Brownian movement. In all three planes the first MSD points show the effect of a wrong tracking ratio mentioned in the section *Simulations* in the chapter *Programming*. All α values are biased through this effect and therefore are greater than 1.

The difference between z axis and the xy plane had two main reasons. When the ventilation and air conditioning were turned on in the laboratory, the water between the objective and the sample was evaporating creating a tension on the coverslip, which is visible as drift in the trajectory. The second effect was the influence of a temperature gradient on the setup caused by the changing temperature due to the sunlight on the black curtains. Both effects are visible as a difference between the 2D MSD plots with a z component (XZ, YZ) and the XY plane. Fig. 4.3 shows the 3D trajectory of a fixed particle. The trajectory is colored from red to green from 0 to 60 seconds. The drift in the Z direction can be easily seen and is in the range of $150nm$. The drift in Y is about $20nm$ and the drift in x even smaller. Since the drift in z is one order of magnitude higher than in the other two directions, the 2D MSD plots for the respectives planes XZ and YZ differ from XY (Fig. 4.2).

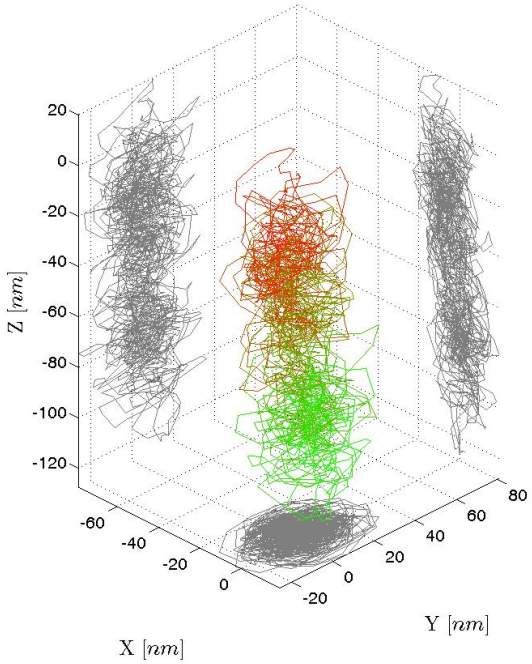

Figure 4.3: Drift of a fixed particle from 0 (red) to 60 seconds (green)

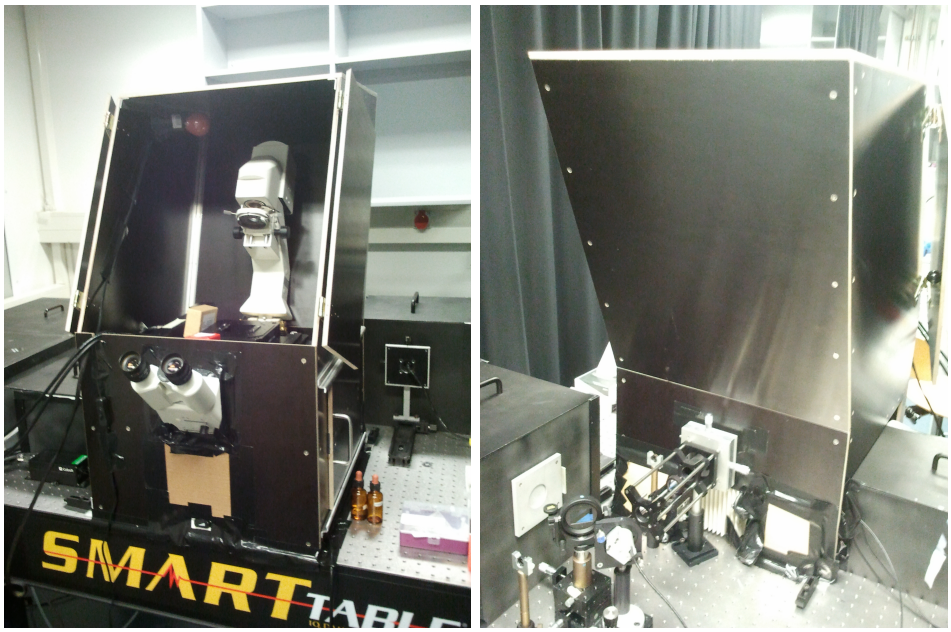

Figure 4.4: Microscopy cage

As explained previously the influence on the beginning of the MSD can be reduced by adjusting the tracking radius manually in SIM FCS. However, the program allows only integer values for the tracking ratio and therefore, this error can not be removed completely. To overcome the drift, the temperature and air flow had to be regulated. To achieve this a cage was build and sealed tightly around the microscope (Fig. 4.4).

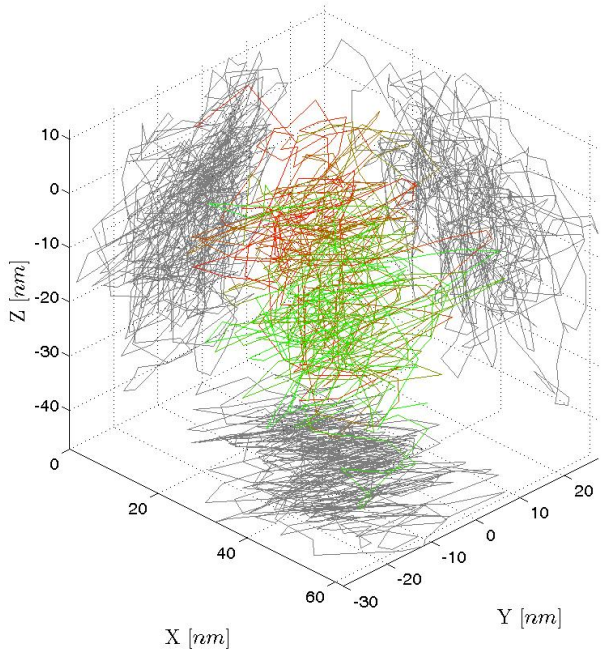

Figure 4.5: No visible drift with microscopy cage from 0 (red) to 30 s (green)

The cage prevents any airflow around the sample holder and the objective and therefore the evaporation of water. Since the airflow was not influencing the setup any more, the air-conditioning and ventilation were switched on again to adjust the temperature of the laboratory. Fig. 4.5 shows the effect of these improvements on the trajectory of a fixed particle. The drift per minute in the Z direction is now reduced by a factor of 4 (Table. 4.1).

Table 4.1: Drift in X,Y and Z with and without the microscopy cage

Drift $[\frac{nm}{min}]$	X	Y	Z
Without cage	16.85	4.34	104.10
With cage and air conditioning	6.34	22.09	25.18

The MSD plot of a free diffusing particle with reduced drift is shown in Fig. 4.6. The difference between the 2D MSD plots is strongly reduced. Table 4.2 shows the diffusion coefficients and α values for the MSD plots in Fig 4.6. However, the effect of the wrong LUT's is still present, which can be seen in the α values slightly bigger than 1. The medium for the tracks was exchanged by a glucose/water mixture since the glycerol/water mixture showed a strange behaviour, which could not be simply explained.

Table 4.2: Diffusion coefficients and α values for Fig. 4.6

	XY	XZ	YZ
Diffusion coefficients $[a.u.]$	9.51	8.44	9.42
α values	1.09	1.14	1.05

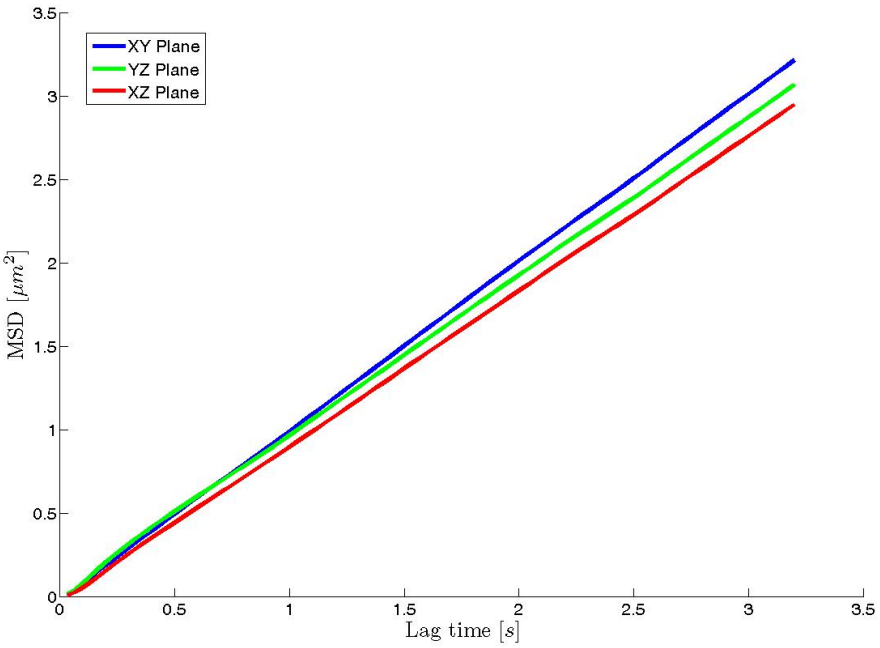

Figure 4.6: 2D MSD plots of a fluorescent bead in a glucose water mixture with reduced drift.

Chapter 5

Conclusion

During this thesis a tracking algorithm was developed and used in simulations to test its performance. In a next step the algorithm will be transferred to the new hardware. The outline for this procedure is described in chapter 3. The FPGA can perform the calculation of the tracking algorithm with higher speed than a normal computer and with a customized program it is possible to decrease the cycle time from the current 32 ms to below 8 ms. By exchanging the piezo mirror with galvano equivalents the cycle time can even be reduced further and so faster particles with higher diffusion coefficients can be tracked. The second disadvantage of the current configuration is the software limited tracking volume. Currently this volume is limited to about 20x20x10μm which corresponds only to about 10% of the available distance in all axes. By increasing this limit to about 50% of the available range the volume would be increased by a factor of 125 which would result in longer tracks and therefore better statistics for a single particle. The tracking volume can be increased further by implementing the movement of an additional X-Y stage in the software, which would be placed on the top of the microscope. This long range tracking could increase the distance in X and Y direction to several mm.

The abilities of the tracking algorithm were investigated in chapter 3. The simulations in this chapter were used to examine the behavior of the tracking algorithm and the effect on MSD plots when changing the tracking ratio and the number of orbit points. The tracking algorithm was able to track particles even with changed values of the tracking ratio and the number of points in the orbit. The error which is introduced by changing those numbers always modifies to first couple of points in the MSD plot. By adjusting those parameters, the error can be reduced iteratively.

The current tracking program SIM FCS uses 128 points for the tracking algorithm but the simulations revealed that only 10 points are required to achieve the accuracy of the LUT. Hence the time to calculate the Fourier coefficients can be reduced. The simulations also showed that the influence of a wrong LUT on MSD plot can not be neglected for short tracks. In SIMFCS the LUT is hidden within the code and can not be changed. However the tracking with different colors requires a LUT for each laser since the width of the PSF is dependent on the excitation wavelength. If the tracks are long enough and enough data points are available, the first 20-30 points of the MSD plot can be discarded since only the beginning of the MSD is affected.

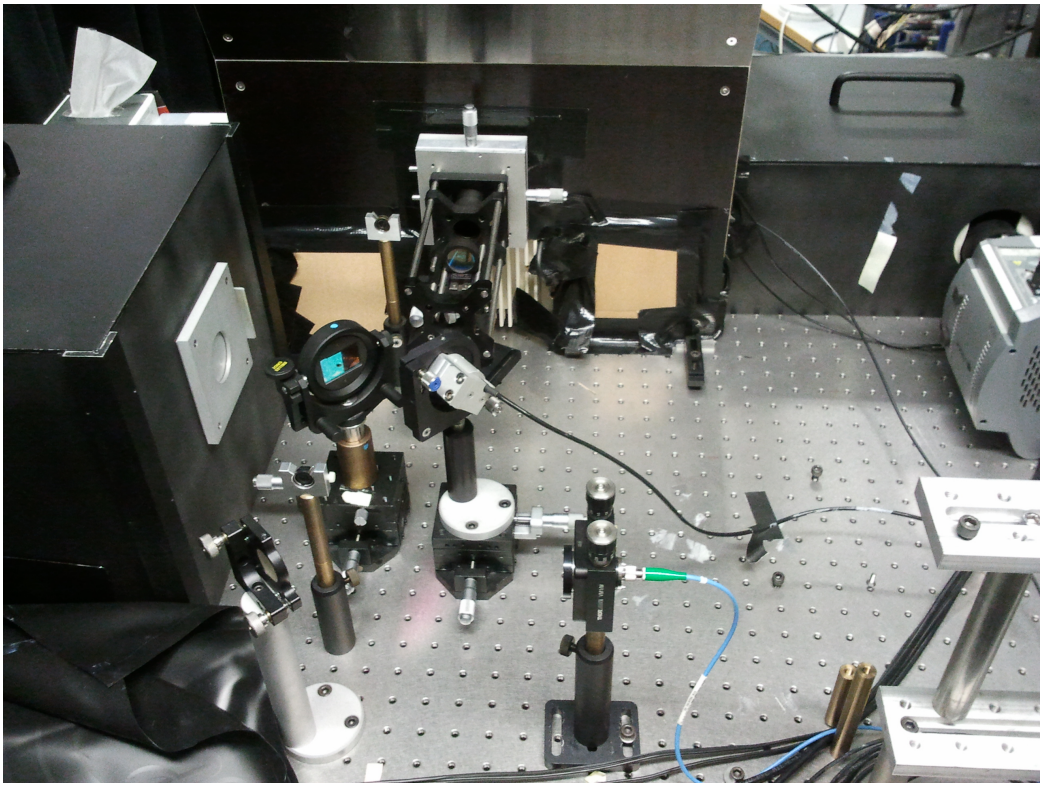

Figure 5.1: Excitation and detection path of the setup

Chapter 4 examines the effect of drift on MSD plots. A sealed cage was constructed around the microscope to be able to use the air-conditioning and achieve a constant temperature in the laboratory. The cage and the air-

conditioning reduced the drift in Z by a factor of 4 and to the same magnitude as in the X and Y directions. In addition the 2D MSDs are more linear and closer to each other. However the air conditioning and the ventilation still directly affect the excitation and detection path and a second cage has to be constructed around these parts to decrease the vibrations caused by the air flow (Fig. 5.1).

The work in this thesis is the base for further improvements to the orbital tracking setup which will be continued after this thesis. The information about tracking and MSD errors of varying tracking ratios and number of orbit points are required to create a stable algorithm with better performances, which can be used for different laser wavelengths and particle sizes. The implementation of the algorithm with the additional long range tracking and faster orbit sampling will pave the way for exciting new experiments, which are not possible today.

Appendix

Abbreviations

MSD	Mean squared displacement
FPGA	field programmable gate array
PSF	point spread function
APD	Avalanche photo diodes
LUT	Look-up table
FWHM	Full width at half maximum
CPU	Central processing unit

Hardware

Name	Model	Company
Piezo Tip-Tilt Platform	S-334.2SL	Physik Instrumente
LVPZT amplifier	E-503.00S	Physik Instrumente
Chassis	E-500.00	Physik Instrumente
Sensor Controller	E-509.S3	Physik Instrumente
Multi Axis Piezo Scanner	-	Physik Instrumente
Objectiv Piezo	MIPOS 100PL CAP	Piezosystems Jena
Piezocontroller	NV 40/1 CL	Piezosystems Jena
Scanning Table	ScanIM 120x100	Maerzhäuser
Positioning System	LSTEP	LANG
FCS Card	-	ISS
3-Axis-Card	-	ISS
Microscope	Axiovert 200	Zeiss
Eye Piece	-	Zeiss
Objective	Plan Apo 60x/1.20 WI	Nikon
Laser (488 nm)	Sapphire 488	Coherent
Laser (561 nm)	JiveTM laser 25 mW lab 561nm	Cobolt AB
Laser (633 nm)	633nm 5mW HeNe laser	Melles Griot
Single Mode Fiber & coupler	-	AMS Technologies
Photon Counting Module	SPCM-AQR-CD-3017	Perkin Elmer
Analogue Input PCI card	PCI-6036E	National Instruments
Analogue Output PCI card	PCI-6733	National Instruments
Connector Block	SCB-68	National Instruments
Shielded cable	SH68-68-EP	National Instruments
Realtime CPU & FPGA	cRIO-9076	National Instruments
Analogue output FPGA	NI 9263	National Instruments

...continued on next page

Name	Model	Company
Digital input FPGA	NI 9402	National Instruments
Acousot Optic Tunable Filter	TF525-250-6-3-GH18A	Gooch & Housego
Cage system, tubes, lenses	-	THORLABS
Dicroic mirrors	-	AHF Analysentechnik
Optical table	-	Newport
Mirror 98,5%	-	AHF Analysentechnik
Triple line beamsplitter	F63-561	AHF Analysentechnik
Emission filter 525/40	F37-521	AHF Analysentechnik
Emission filter 593/40	F37-593	AHF Analysentechnik
Emission filter 695/100	-	Chroma
Beamsplitter 50/50 VIS	-	AHF Analysentechnik

Bibliography

[1] Robert Hooke. *MICROGRAPHIA*. The Royal Society of London for Improving Natural Knowledge, 1665.

[2] J. D. Watson and F. H. C. Crick. Molecular structure of nucleic acids: A structure for deoxyribose nucleic acid. *Nature*, 171(4356):737–738, 1953.

[3] E. Abbe. Beitraege zur theorie des mikroskops und der mikroskopischen wahrnehmung. *Archiv fuer Mikroskopische Anatomie*, 9(1):413–418, 1873.

[4] G. G. Stokes. On the change of refrangibility of light. *Philosophical Transactions of the Royal Society of London*, 142:463–562, 1852.

[5] Joseph R. Lakowicz. *Principles of Fluorescence Spectroscopy*. Springer US, 4th printing. edition, 2010.

[6] Nikolaus Naredi-Rainer. *Multi Parameter Fluorescence Spectroscopy - Setup, Assemply and Applications*. 2008.

[7] J. Ingenhousz. *Vermischte schriften physisch medicinischen inhalts*. KrauÃ, 1782.

[8] Robert Brown. A brief account of microscopical observations made in the month of june, july aug., 1827, on the particles contained in the pollen of plants; and on the general existence of active molecules in organic inorganic bodies. *Phil. Mag.*, 4(21):161–173, 1828.

[9] A. Einstein. Ueber die von der molekularkinetischen theorie der waerme geforderte bewegung von in ruhenden fluessigkeiten suspendierten teilchen. *Annalen der Physik*, 322(8):549–560, 1905.

[10] Howard C. Berg. How to track bacteria. *Review of Scientific Instruments*, 42(6):868–871, 1971.

[11] Klaus Schaetzel, Wulf-Gerd Neumann, Juergen Mueller, and Bernd Materzok. Optical tracking of single brownian particles. *Appl. Opt.*, 31(6):770–778, 1992.

[12] Adam E. Cohen and W. E. Moerner. Controlling brownian motion of single protein molecules and single fluorophores in aqueous buffer. *Opt. Express*, 16(10):6941–6956, 2008.

[13] Aurelie Dupont and Don C. Lamb. Nanoscale three-dimensional single particle tracking. *Nanoscale*, 3(11):4532–4541, 2011.

[14] H. P. Kao and A. S. Verkman. Tracking of single fluorescent particles in three dimensions: use of cylindrical optics to encode particle position. *Biophys J*, 67(3):1291–300, 1994.

[15] Michael Speidel, Alexandr Jona, and Ernst-Ludwig Florin. Three-dimensional tracking of fluorescent nanoparticles with subnanometer precision by use of off-focus imaging. *Opt. Lett.*, 28(2):69–71, 2003.

[16] Inge M. Peters, Bart G. de Grooth, Juleon M. Schins, Carl G. Figdor, and Jan Greve. Three dimensional single-particle tracking with nanometer resolution. *Review of Scientific Instruments*, 69(7):2762–2766, 1998.

[17] Adam E. Cohen and W. E. Moerner. Method for trapping and manipulating nanoscale objects in solution. *Applied Physics Letters*, 86(9):093109, 2005.

[18] Guillaume A. Lessard, Peter M. Goodwin, and James H. Werner. Three-dimensional tracking of individual quantum dots. *Applied Physics Letters*, 91(22):224106, 2007.

[19] J. Enderlein. Tracking of fluorescent molecules diffusing within membranes. *Applied Physics B: Lasers and Optics*, 71(5):773–777, 2000.

[20] Katarina Kis-Petikova and Enrico Gratton. Distance measurement by circular scanning of the excitation beam in the two-photon microscope. *Microscopy Research and Technique*, 63(1):34–49, 2004.

[21] Yoshihiko Katayama. *3D Particle Tracking in Cellular Systems*. Hieronymus Verlag, 2009.